Nano Research

Open Access

Research Article

Low-thermal budget fabrication of two-dimensional Schottky diodes for broadband convolutional processing

Zichao Han[1,§], Shijia Tian[1,§], Han Wang[1], Weihui Sang[1], Yang Gan[1], Yi Cao[2,3], Feixia Tan[2,3], Honghong Li[2,3], Tinghao Wang[2,3], Yuan Yu[1], Wenyu Songlu[2,3], Yue Wang[1], Tao Liu[1] ✉, and Du Xiang[2,4] ✉

[1] *Shanghai Frontiers Science Research Base of Intelligent Optoelectronics and Perception, Institute of Optoelectronics and Department of Materials Science, Fudan University, Shanghai 200433, China*
[2] *State Key Laboratory of Integrated Chips and Systems, Frontier Institute of Chip and System, Fudan University, Shanghai 200438, China*
[3] *School of Microelectronics, Fudan University, Shanghai 200433, China*
[4] *Zhangjiang Fudan International Innovation Center, Fudan University, Shanghai 200433, China*
§ *Zichao Han and Shijia Tian contributed equally to this work.*

Cite this article: *Nano Research*, **2025**, *18*, 94907049. https://doi.org/10.26599/NR.2025.94907049

ABSTRACT: In-sensor broadband convolutional processing (BCP) holds great significance to the advancement of high-precision image recognition for remote sensing and environmental monitoring. Two-dimensional (2D) heterostructures offer abundant band alignment configurations with electrical tunability, which is promising to implement the in-sensor BCP at hardware level. Huge efforts have been devoted to developing 2D heterostructures based intelligent edge devices for BCP, which however either lack the potential for scalability and reproducibility, or require high processing temperature. Here, we demonstrate a $PtSe_2/WSe_2$ heterostructure based Schottky diode fabricated by using thermal-assisted conversion (TAC) technique, which converts the pre-deposited Pt films into $PtSe_2$ via the controllable selenization process with complementary metal-oxide-semiconductor (CMOS) back-end-of-line (BEOL) compatible thermal budget. The TAC-$PtSe_2$ in various thicknesses demonstrate high crystalline nature and low contact resistance (425 Ω·μm), facilitating an atomically sharp interface and gate-tunable band alignment. Such characteristics give rise to polarity-changeable built-in electric field, resulting in a remarkable rectification ratio approaching ~ 10^5. Moreover, the positive–negative switching of the photoresponse with linear intensity dependence is achieved across a wide spectrum from ultraviolet to near-infrared light, which is desirable in constructing various convolution kernels for BCP tasks. A hyperspectral remote sensing image is adopted to demonstrate the BCP operations including edge detection and sharpness, where the outputs are of comparable quality with the simulated results. Our work envisions a CMOS-compatible approach for fabricating 2D Schottky diodes with tunable band alignment, offering a viable route for the scalable hardware implementation of broadband image processing units.

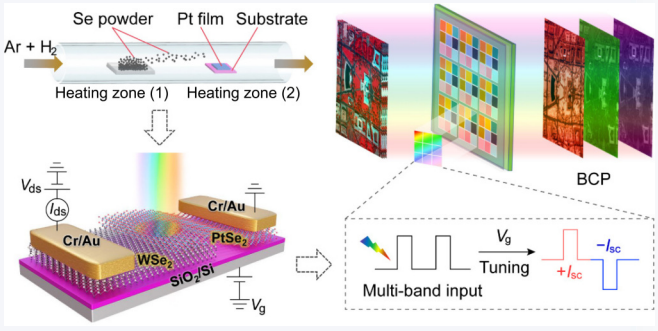

KEYWORDS: broadband convolutional processing, thermal-assisted conversion, two-dimensional heterostructures, photovoltaic effect, Schottky diodes

1 Introduction

Broadband convolutional processing (BCP) is a typical technique for extracting key features in target input patterns, especially for the remote sensing images containing multi-band information ranging from ultraviolet to infrared light [1–5]. Inspired by the biological retina system, the in-sensor BCP has been further developed, where the analogue image information is captured and processed in the vision sensors, which is essential to reduce the energy cost and time latency [6–9]. However, implementing the sensing and processing functions simultaneously in conventional complementary metal-oxide-semiconductor (CMOS) based platform remains challenging, arising from the intrinsic nature of the separated front-end silicon (Si) photodiodes and back-end digital processors [10]. On the other

Received: July 19, 2024; **Revised:** September 10, 2024
Accepted: September 23, 2024

✉Address correspondence to Tao Liu, liu_tao@fudan.edu.cn; Du Xiang, xiang_du@fudan.edu.cn

hand, the current Si and indium-gallium-arsenide (InGaAs) based photodiodes possess fixed bandgaps and doping profiles that are specific to certain wavelength bands, thus yielding limitations in acquiring broadband information [11]. Additionally, integrated BCP hardware requires continuous downscaling of functional units with high power efficiency, which is however an obvious obstacle in CMOS based development route [12].

Two-dimensional (2D) heterostructures, formed by artificially stacking different 2D layered materials with atomic-level flatness of surface and interface, offer tremendous possibilities in realizing downscaled in-sensor BCP hardware due to their extraordinary capability to integrate and process optical/electrical signals [13–20]. The intelligent edge devices are constructed on the basis of designing bandgap alignment features while incorporating optical/electrical modulations, which produces highly-tunable photoresponse that allows multifunctional applications, including reconfigurable neuromorphic visual sensors [21], polarization-sensitive and broadband photodetectors for image recording and processing [22, 23], light-tunable memory matrix [24], as well as miniaturized computational spectrometers [25]. Nevertheless, to achieve the target 2D heterostructures, mechanical stacking and chemical vapour deposition (CVD) techniques are generally employed, which however either lack the scalability and reproducibility, or require high processing temperature beyond the thermal budget of Si based manufacturing techniques [26–29]. To promote the innovations of 2D photodiodes for in-sensor BCP with CMOS integration potential, it is crucial to develop highly scalable heterostructure fabrication strategies with back-end-of-line (BEOL) compatibility.

Thermal-assisted conversion (TAC), a CMOS-compatible technique possessing low thermal budget, has been identified as a potential pathway to synthesize 2D materials and heterostructures with appreciable scalability and mass-production capability [30–33]. The material integrity and device functionality of the TAC-synthesized 2D materials can be preserved, as comparing to their single crystalline counterparts [34]. This envision TAC method is a viable approach for realizing diverse 2D heterostructures with robust sensing and processing functionalities, and is promising for the implementation of BCP tasks. Multilayer/bulk $PtSe_2$ is a typical van der Waals material exhibiting metallic nature with robust ambient stability [35–38]. However, the melting/sublimation temperature of Pt is inaccessible by using solid-state material synthesis processes, making the relevant compound difficult to be synthesized [39], and thus compromising its application potential. On the other hand, WSe_2 possesses ambipolar transport nature [40], where the band alignment feature with TAC-$PtSe_2$ can be effectively tuned through the application of different gate voltages, generating photovoltaic response with both positive and negative polarities. This is crucial for the construction of gate-tunable convolutional kernels, which is beneficial to the implementation of image processing algorithm. Here, we report a TAC-assisted synthetic strategy of $PtSe_2$ through controllable selenization of Pt films, which can be utilized to fabricate the TAC-$PtSe_2$/WSe_2 heterostructure with high lattice quality and preserved material properties. Owing to the metallic behaviour of TAC-$PtSe_2$ and the ambipolar transport feature of WSe_2, the heterojunction device functions as a Schottky diode with gate-configured band alignment, which facilitates the polarity-tunable photovoltaic response with wide spectrum sensing capability. These characteristics allow for the perception of optical information with simultaneous construction of broadband convolutional kernels for various operations. We perform edge detection and sharpness on the remote sensing images to demonstrate the in-sensor BCP functions, which generates the output patterns with comparable quality to the software simulated results.

2 Experimental section

2.1 Synthesis of 2D $PtSe_2$ through TAC technique

Standard electron beam lithography (EBL) was employed to define the Pt patterns on the SiO_2/Si substrates. Pt films with different thicknesses were then deposited using electron beam evaporation (EBE). The TAC process was conducted inside a two-zone tube furnace. The substrate was placed in the second heating zone (set at 400 °C), while the Se powder (99.5%, Sigma Aldrich) was located in the first heating zone (set at 220 °C). The flow rate of the mixed carrying gas Ar/H_2 (9:1) was set to 50 sccm. The reaction time was set to 1–2 h depending on the Pt layer thickness.

2.2 Fabrication of the TAC-$PtSe_2$ transistors and the TAC-$PtSe_2$/WSe_2 heterostructure device

For the fabrication of TAC-$PtSe_2$ transistors, the standard EBL was used to define the electrodes, which were then metallized by depositing Cr/Au (5/50 nm) using EBE. In the case of the heterostructure devices, WSe_2 (HQ graphene) was first exfoliated on the SiO_2/Si substrates, after which the Pt patterns were defined and deposited using the same EBL and EBE techniques. Cr/Au (5/50 nm) was deposited using EBE as the electrodes.

2.3 Electrical transport and optoelectronic measurements

The as-fabricated devices were wire-bonded onto a chip carrier and loaded into a high vacuum chamber for characterization (pressure below 10^{-6} mbar). Electrical experiments were conducted at room temperature using a PDA FS Pro PX600 semiconductor parameter analyzer. The optoelectronic measurements were carried out by using three laser beams with different wavelengths (385, 520, and 980 nm). A signal generator was integrated with the lasers to generate the light pulse. The laser power was calibrated using THORLABS GmbH (PM 100A) power meter.

3 Results and discussion

3.1 Preparation and characterization of 2D TAC-$PtSe_2$

The upper panel of Fig. 1(a) schematically illustrates the TAC process. The pre-deposited Pt patterns are annealed at 400 °C in a selenium (Se)-rich environment, which can be directly converted into $PtSe_2$ crystals that possess a 1T lattice structure as shown in the lower panel of Fig. 1(a) [37, 39]. According to the processing time in our experiment, the range of thermal budget is determined to be 4.04×10^4 to 8.08×10^4 Kelvin·minutes, which is comparable to that of the silicon-based CMOS BEOL process [41]. The thicker Pt films generally require longer reaction time to ensure its completed transformation into the $PtSe_2$ (Fig. S1 in the Electronic Supplementary Material (ESM)). The thickness of the TAC-$PtSe_2$ scales linearly with the Pt seeding layers, giving rise to an expansion factor ranging from 3.5 to 4 (Fig. 1(b)). The factor is consistent with that of the previous reports, validating the efficiency and completeness of the selenization process [42]. The crystallinity

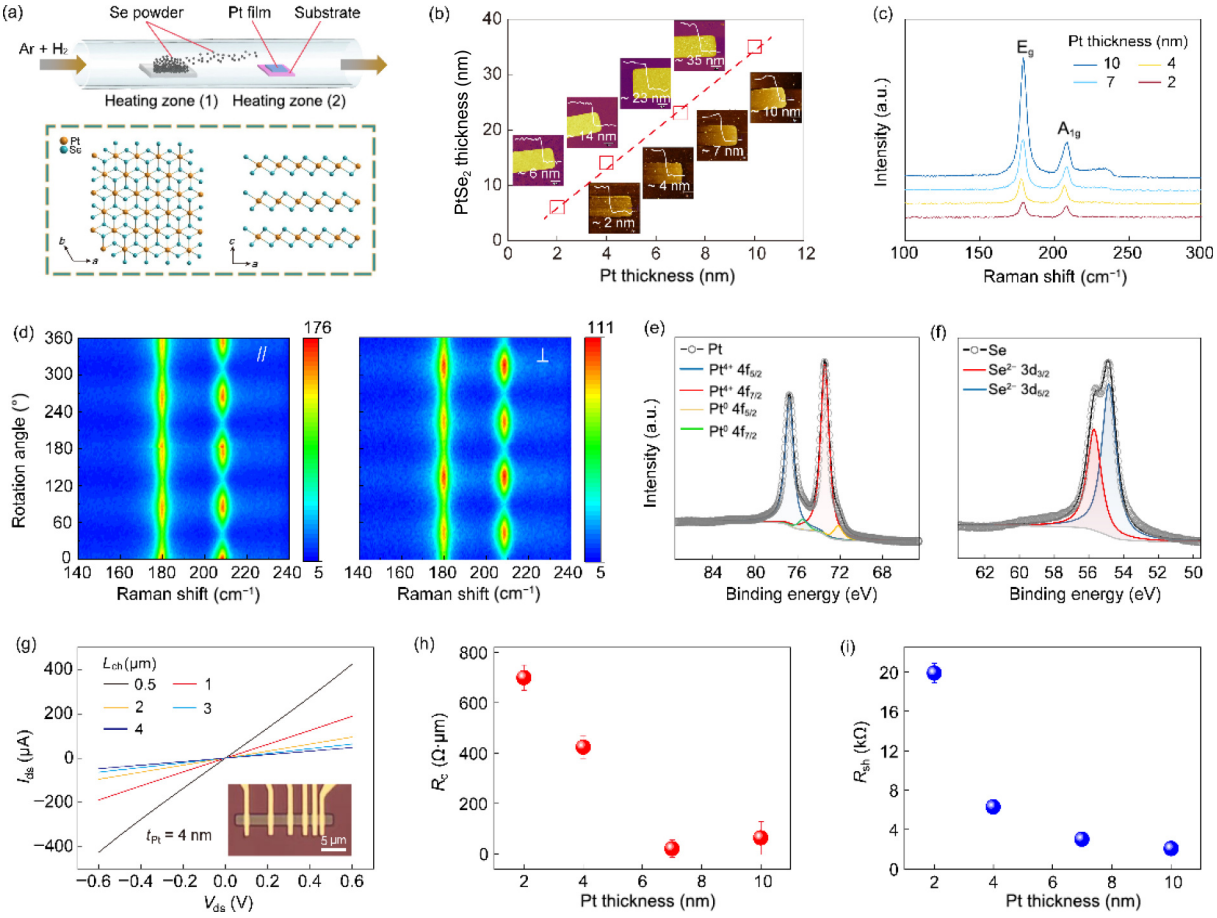

Figure 1 Synthesis and characterization of 2D TAC-$PtSe_2$. (a) Upper panel: Schematic of the TAC process. Lower panel: Schematic of the 1T structure of $PtSe_2$ lattice. The Pt and Se atoms are in yellow and blue color, respectively. (b) Thickness scaling of TAC-$PtSe_2$ in terms of the initial Pt thickness. Insets show the AFM characterizations of the Pt and the corresponding TAC-$PtSe_2$ films of different thickness. (c) Raman spectra of the TAC-$PtSe_2$ samples prepared using the Pt films with different thickness. (d) Polarized Raman intensity mapping of the TAC-$PtSe_2$ film in parallel (left) and perpendicular (right) polarization configurations, respectively. XPS spectra of (e) Pt 4f and (f) Se 3d core levels. The thickness of the pre-deposited Pt layer is 4 nm. (g) Output curves of the TAC-$PtSe_2$ transistors with different channel lengths (0.5, 1, 2, 3, and 4 μm). Inset shows the corresponding optical image. Scale bar is 5 μm. Extracted values of (h) R_c and (i) R_{sh} as a function of the initial Pt thickness.

nature of the TAC-$PtSe_2$ with different initial Pt thickness is characterized by using the Raman spectroscopy, where all the resultant crystals exhibit the E_g (178 cm^{-1}) and A_{1g} (207 cm^{-1}) characteristic peaks (Fig. 1(c)). It is noted that the intensity of the Raman peaks is gradually enhanced as increasing the thickness of the Pt seeding layer, suggesting that the selenization reaction occurs throughout the entire depth of the deposited Pt patterns. Moreover, the TAC-$PtSe_2$ demonstrates outstanding uniformity as verified by the Raman mapping of the characteristic peaks (Fig. S2 in the ESM). We further study the phonon vibration anisotropy of the TAC-$PtSe_2$ using angle-resolved polarization Raman spectroscopy (ARPRS). Taking 4 nm Pt layer as an example (Fig. 1(d), and Fig. S3 in the ESM), the A_{1g} peak in the $PtSe_2$ displays 4-lobed shape in both parallel and perpendicular polarization configurations with respect to the incident laser orientation, while the E_g peak exhibits much weaker angle-dependence in both directions, which is consistent with those reported in the single-crystal $PtSe_2$ [43]. Polarized Raman mapping of $PtSe_2$ with varied Pt seeding layers are summarized in Table S1 in the ESM, where the similar features are observed as those shown in Fig. 1(d).

Furthermore, the X-ray photoelectron spectroscopy (XPS) measurements are carried out to confirm the chemical composition of the TAC-$PtSe_2$. It is also used to evaluate the completeness of the TAC reaction. We propose that the reaction is completed for the case that the content of elemental Pt is below 10%, where the Pt residue does not affect the electrical properties of the TAC derived $PtSe_2$. Figures 1(e) and 1(f) show the Pt 4f and Se 3d core level binding energy of the $PtSe_2$ sample selenized from a 4 nm Pt layer. The Pt 4f core level consists of two main peaks located at 76.8 and 73.5 eV, corresponding to the Pt^{4+} $4f_{5/2}$ and Pt^{4+} $4f_{7/2}$, respectively. It is noted that there are two additional peaks emerging with lower binding energy located at 75.5 and 72.3 eV, respectively, which can be attributed to the unreacted Pt metal residues. Nevertheless, based on the following electrical and optical characterizations, it can be concluded that such minimal amount of Pt residue (~ 8%) has limited impact on the overall physical properties of the TAC-$PtSe_2$, which is essential to maintain its application potential. On the other hand, the deconvolution of Se 3d core level generates two peaks located at 55.7 and 54.8 eV, which can be assigned to the Se^{2-} $3d_{3/2}$ and Se^{2-} $3d_{5/2}$, respectively. The absence of peak Se^0 at the binding energy of ~ 56.8 eV indicates the complete reaction of Se during the selenization process [44]. The consistent Pt and Se core levels are also observed in other TAC-$PtSe_2$ samples selenized by the Pt seeding layer with various thicknesses (Fig. S4 in the ESM). These results envision TAC as an effective and reliable approach for the synthesis of 2D transition metal dichalcogenides (TMDs),

particularly for those containing metals with high melting temperatures, owing to its low thermal budget that assures excellent CMOS BEOL-compatibility.

The electrical transport properties of the TAC-$PtSe_2$ are then quantified by using the transfer length method (TLM) to evaluate its potential for the device applications. Figure 1(g) shows the current–voltage (I_{ds}–V_{ds}) characterizations of the TAC-$PtSe_2$ with various channel lengths using 4 nm Pt as the seeding layer, where the linear features indicate the excellent Ohmic contacts. The contact resistance (R_c) is extracted to be 425 Ω·μm (Figs. S5 and S6 in the ESM), while the sheet resistance (R_{sh}) is around 6.32 kΩ (see the ESM for details). The TLM based measurements of other TAC-$PtSe_2$ samples with different Pt thicknesses are illustrated in Fig. S7 in the ESM, where the corresponding R_c and R_{sh} are also demonstrated. The R_c and R_{sh} of the TAC-$PtSe_2$ exhibit a significant decrease from 700 to 21 Ω·μm and 19.9 to 2.97 kΩ as the thickness of pre-deposited Pt layer increases from 2 to 7 nm, followed by a gradual saturation as further increasing the Pt thickness to 10 nm (Figs. 1(h) and 1(i)). This can be attributed to the thickness-dependent semiconducting-to-metallic transition in $PtSe_2$ as that observed in the single crystalline counterpart [45]. To further verify the semiconducting/metallic nature of the TAC-$PtSe_2$, we characterize their gate-dependent output and transfer properties (Fig. S8 in the ESM). The channel current of the thinnest TAC-$PtSe_2$ demonstrates marginal gate-dependency, while metallic behaviour is observed in all other thicker samples, confirming the thickness-determined evolution of the electrical transport characteristics of the TAC-$PtSe_2$.

3.2 Gate-tunable electrical transport and photovoltaic performance

The metallic nature of thick TAC-$PtSe_2$ is favourable in designing the semiconductor–metal heterojunctions for Schottky diode applications. The diode in 2D heterostructure is schematically illustrated in Fig. 2(a) with the corresponding optical image shown in Fig. S9 in the ESM. The multilayer WSe_2 is exfoliated as the semiconducting channel, followed by the deposition of the Pt layer (6 nm) with the TAC process (see the Experimental section for details of the device fabrication). The $PtSe_2$ and WSe_2 channels are connected to the source and drain terminals, respectively. The cross-sectional transmission electron microscope (TEM) image reveals a clear interface between the TAC-$PtSe_2$ and WSe_2, while the layered crystallinity with appreciable lattice integrity is preserved for both materials (Fig. 2(b)). Note that the thickness of the TAC-$PtSe_2$ is

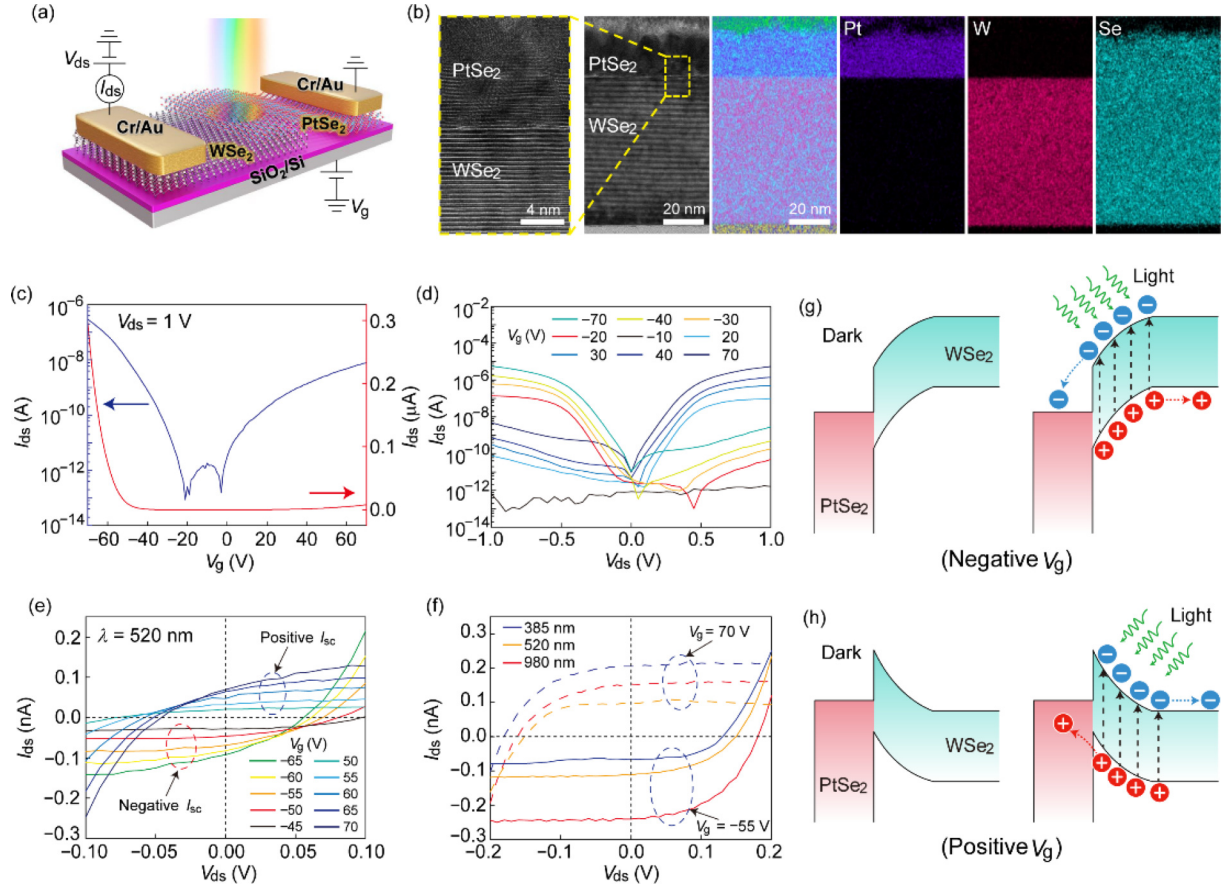

Figure 2 TAC-$PtSe_2$/WSe_2 heterojunction device with gate-tunable photovoltaic response. (a) Schematic of the TAC-$PtSe_2$/WSe_2 heterostructure device. (b) Cross sectional TEM and EDS images of the TAC-$PtSe_2$/WSe_2 heterostructure. The thicknesses of TAC-$PtSe_2$ and WSe_2 are 21.1 and 71.6 nm, respectively, with a scale bar of 20 nm. (c) Transfer characteristics of the device under V_{ds} = 1 V. (d) The V_g-dependent output characteristics of the device. V_g ranges from −70 to 70 V. (e) The photovoltaic response of the device under the modulation of different V_g ranging from −65 to 70 V. The wavelength of the light is 520 nm with a power density of 11.05 mW·cm^{-2}. (f) Polarity switching of the photovoltaic effects under light illumination with different wavelengths of 385, 520, and 980 nm, respectively. The respective power densities are 12.48, 9.06, and 84.9 mW·cm^{-2}. Schematic illustration of the band alignment features of the TAC-$PtSe_2$/WSe_2 heterostructure under (g) negative and (h) positive V_g. The red/blue balls represent holes/electrons. The black arrow indicates the electron–hole pair separation under light illumination, while the red/blue arrows refer to the flow directions of holes/electrons driven by the build-in electric fields.

measured to be 21.1 nm, corresponding to an expansion factor of 3.5 that is consistent with the scaling trend obtained in Fig. 1(b). On the other hand, the vertical elemental composition of the heterostructure is verified by the energy-dispersive spectrometer (EDS), which demonstrates negligible atomic inter-diffusion, further verifying the viability of the TAC process for the fabrication of the Schottky diode. Figure S10 in the ESM depicts the Raman characterizations of both the junction and the individual regions of the heterostructure. It is noted that all the characteristic peaks of the WSe_2 in the junction regime (i.e., E^1_{2g} mode at 250 cm^{-1}, A_{1g} mode at 258 cm^{-1}, and B^1_{2g} mode at 310 cm^{-1}) are preserved without noticeable change, suggesting that the intrinsic properties of WSe_2 can be largely maintained after the TAC treatment, and thus ensuring its functionality in the fabricated Schottky diode. The TAC approach is an effective method for the synthesis of 2D materials, which demonstrates the potential in wafer-scale manufacturing with the advantages of artificial patterning, low thermal budget, and CMOS compatibility. Therefore, it is promising to achieve the heterostructure array with satisfactory performance in large scale through employing the all-TAC fabrication procedure, which involves the deposition of different target metals, followed by careful optimization of the selenization parameters.

We then characterize the electrical transport behaviour and photovoltaic response of the device. The transfer curves of the device at bias V_{ds} = 1 V are illustrated in Fig. 2(c), which exhibits hole-dominated ambipolar characteristics. Since the thick TAC-$PtSe_2$ possesses gate-independent conductance, the overall transport features are mainly determined by the WSe_2 channel. Figure 2(d) depicts the gate (V_g) modulated output curves of the device, in which the typical signatures of a diode are observed. It is noted that the rectifying output curves are reversed under the modulation of the positive and negative gates, which is due to the ambipolar nature of the WSe_2 channel. The extracted rectification ratio of the diode as a function of V_g is illustrated in Fig. S11 in the ESM. The ratio is significantly enhanced as increasing the gate in both the positive and negative directions, which approaches ~ 10^5 at V_g = ±70 V, arising from the improved Schottky barrier height and built-in electric field at the $PtSe_2/WSe_2$ interface for electron and hole conductions.

Such Schottky diode configuration enables photovoltaic response under zero V_{ds} upon light illumination, as shown in Fig. 2(e). A positive (negative) short-circuit current (I_{sc}) with different magnitudes is spontaneously generated in the irradiated device under positive (negative) V_g, illustrating the tunability of the bipolar photovoltaic behaviour through modulating the interfacial Schottky barrier in the heterostructure device. To further verify that I_{sc} is mainly contributed by the junction induced photovoltaic effect, we monitor I_{sc} by illuminating the different sites of the device (Fig. S9 and Table S2 in the ESM). The spontaneous photocurrent appears only within the junction region, thus eliminating the contributions from the individual constituent materials. We propose a model to capture the gate-dependent photovoltaic response of the diode, as schematically illustrated in the energy band alignment diagram in Figs. 2(g) and 2(h). The Fermi level of WSe_2 undergoes a downshift at negative V_g, forming a build-in electric field that facilitates the separation of the photo-generated electrons–hole pairs in WSe_2 under illumination. The holes and electrons flow to the WSe_2 and $PtSe_2$ channel respectively, generating a negative spontaneous photocurrent. Conversely, the direction of the build-in electric field is reversed under positive V_g, thus giving rise to a positive photovoltaic response. Moreover, the band offset increases with increasing V_g toward both polarities, which induces higher Schottky barrier height as well as the stronger build-in electric field for the more efficient separation of the photo-generated electron–hole pairs, thus resulting in the enhanced I_{sc}.

The significant photovoltaic effect is identified in broadband spectrum ranging from 385 (ultraviolet, UV) to 980 nm (near-infrared, NIR). The polarity switching of I_{sc} is consistently observed in all different wavelengths, as V_g changes from 70 to −55 V (Fig. 2(f)). The response speed of the device is also characterized, where both the rising and decaying time are within a range of 1 to 6 ms for both the positive and negative I_{sc} (Table S3 in the ESM), suggesting its fast operation speed. In addition, the stability of the photovoltaic response is investigated, where I_{sc} is nearly maintained during the application of 100 consecutive light pulses on the device at different wavelengths, indicating its robust cyclic endurance (Table S4 in the ESM). Note that the photoresponse at all the wavelength is due to the photo-excitation in WSe_2. The thickness of the WSe_2 flake used for device fabrication is around 71.6 nm, approaching the bulk state with bandgap of ~ 1.0 eV [46, 47]. This is even lower than the smallest photon energy of 980 nm laser (~ 1.27 eV), thus ensuring the effective light absorption that generates photon-excited carriers. Moreover, we noticed that the photoresponsivity and response speed of our device is lower than that reported before using exfoliated crystals [48]. This can be attributed to the polycrystalline nature of the TAC-$PtSe_2$, where both the carrier mobility and electrical conduction are poorer than those of the single crystalline counterpart. Additionally, we observe that the selenization process could also influence the electrical transport properties of the WSe_2 flakes (Fig. S12 in the ESM). The device current with selenization is decreased by nearly one order of magnitude for both the electron- and hole-conduction branches comparing to that of the pristine counterparts without selenization, which could be due to the introduction of the Se defects in the WSe_2 flakes during the selenization process at relatively high temperature. The poorer quality of the TAC-$PtSe_2$ and WSe_2 samples with certain defects induced scattering centres could degrade the transport and collection of the photo-generated carriers, giving rise to the lower responsivity and longer response time.

Moreover, it is worth noting that the gate-tunable photovoltaic characteristics with consistent response speed and cyclic endurance can be extended to the 1064 nm wavelength band (Figs. S13–S15 in the ESM), which is constrained by our experimental equipment but not limited by the intrinsic working range of the device. We thus propose that the Schottky junction device might possess appreciable photoresponse even in the mid-infrared bands, suggesting the possibility of further extending the operation wavelength [49, 50].

3.3 Construction of convolution kernels using polarity-tunable photoresponsivity

The implementation of in-sensor BCP requires the simultaneous perception of optical signals and the construction of convolution kernels containing both positive and negative elements with certain relations in hardware optoelectronic devices [51]. Specifically, high-quality broadband information acquisition requires linearly related photocurrent and the incident light power at all the relevant wavelengths, while controllable positive/negative photoresponse with typical span and proportionality across a wide spectrum is necessary to construct the corresponding kernel matrices. The TAC-

$PtSe_2/WSe_2$ heterostructure demonstrates gate-tunable photovoltaic response in a wide spectrum, which is promising for the BCP applications. To further validate the potential of employing the heterostructure device to execute the BCP tasks, we comprehensively characterize the photocurrent as functions of both V_g and light intensity at different wavelengths. Figures 3(a)–3(c) explicitly illustrate the negative-to-positive transition of I_{sc} as increasing V_g from −70 to 70 V at the wavelengths of 385, 520, and 980 nm with the same power density. This is consistent with the output curves of the device under light illumination shown in Fig. 2(e).

I_{sc} as a function of laser power under various wavelengths at V_g = ±60 V is presented in Figs. 3(d)–3(f). The equation $I_{sc} \propto P^{\alpha}$ is used to fit the experimental data, where all the values of α are close to 1, indicating an excellent linear relationship between I_{sc} and the laser power. Such high linearity ensures the high-quality perception of image information for the BCP tasks. The detailed gate-driven photocurrent evolution trends at different wavelengths are presented in Figs. 3(g)–3(i), where all the negative–positive photoresponsivity (R_{sc}) transitions occur at $V_g \sim -10$ V, further confirming that such phenomenon is primarily governed by V_g controlled doping profile (i.e., the band alignment feature) of the heterojunction, with negligible effect arising from the irradiation conditions. We note that R_{sc} deviates from the perfect linear relationship with respect to V_g, which however, does not affect the overall monotonic evolution trend and thus still allows for the construction of various convolution kernels for multiple types of the BCP. We also fabricated the heterostructure devices using the WSe_2 flakes with thinner thicknesses, and summarized their photovoltaic performance as a function of V_g, as shown in Fig. S16 in the ESM. These devices exhibit lower responsivity for both the positive and negative photoresponse, with higher degree of asymmetry and device-to-device variation. These characteristics make the devices using thin WSe_2 flakes difficult to satisfy the requirement for constructing the convolutional kernels in implementing the BCP task. Therefore, we still choose thick WSe_2 flakes for the demonstration of BCP functions, which exhibit more stable and consistent device properties.

3.4 Implementation of in-sensor BCP task

The implementation of BCP is shown in the left panel of Fig. 4(a). The device perceives the broadband optical signals, generating pre-processed images at different wavelength bands through the convolutional operations. A single read-out operation is adopted to realize the simultaneous image sensing and pre-processing, as shown in the right panel of Fig. 4(a). The input hyperspectral image

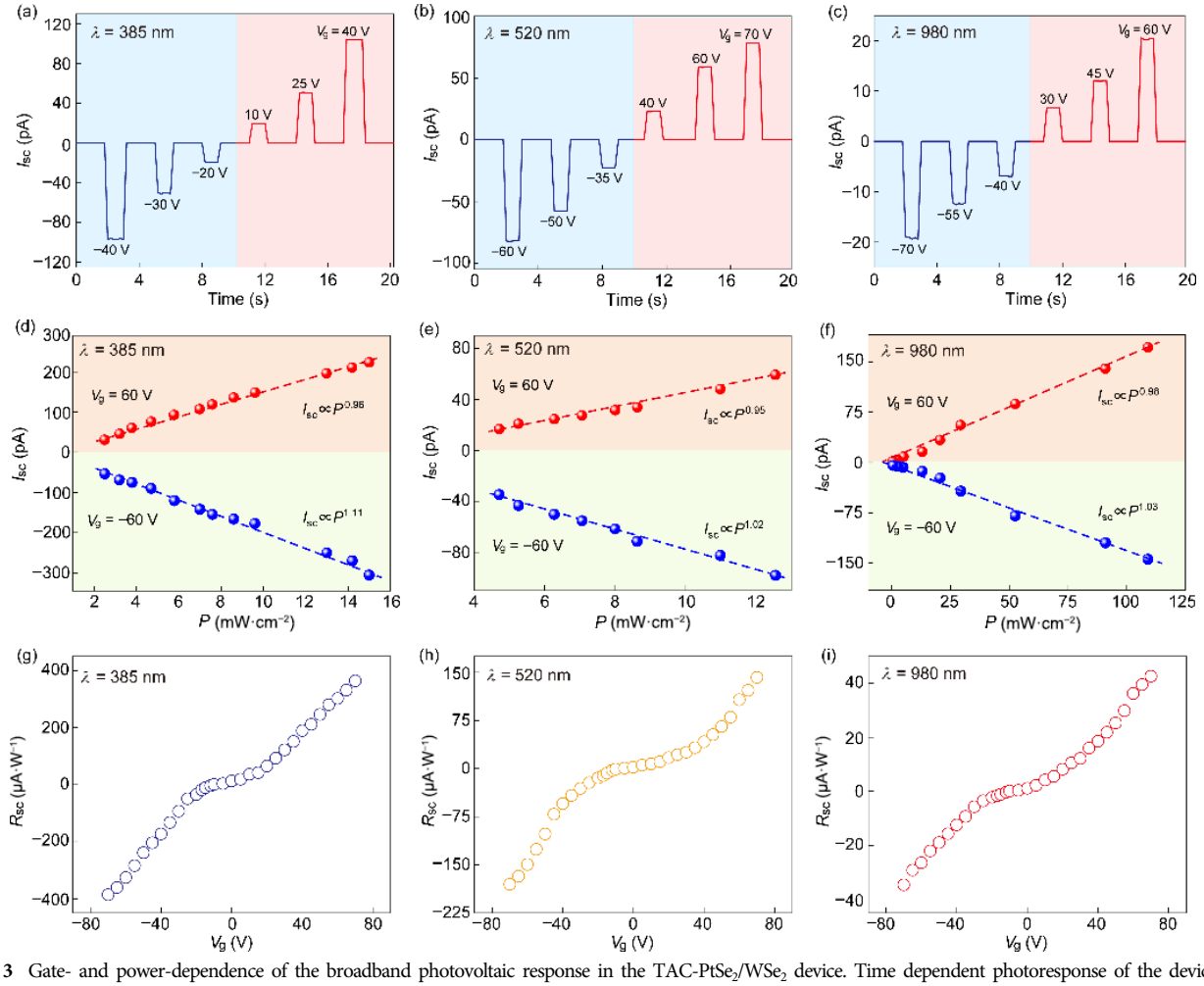

Figure 3 Gate- and power-dependence of the broadband photovoltaic response in the TAC-$PtSe_2/WSe_2$ device. Time dependent photoresponse of the device with changing V_g under different wavelengths from UV to NIR of (a) 385, (b) 520, and (c) 980 nm. The power density is set as 10.98 mW·cm^{-2}. The positive and negative I_{sc} versus the laser power at V_g = ±60 V under different wavelengths of (d) 385, (e) 520, and (f) 980 nm. Photoresponsivity as a function of V_g with different wavelengths of (g) 385, (h) 520, and (i) 980 nm.

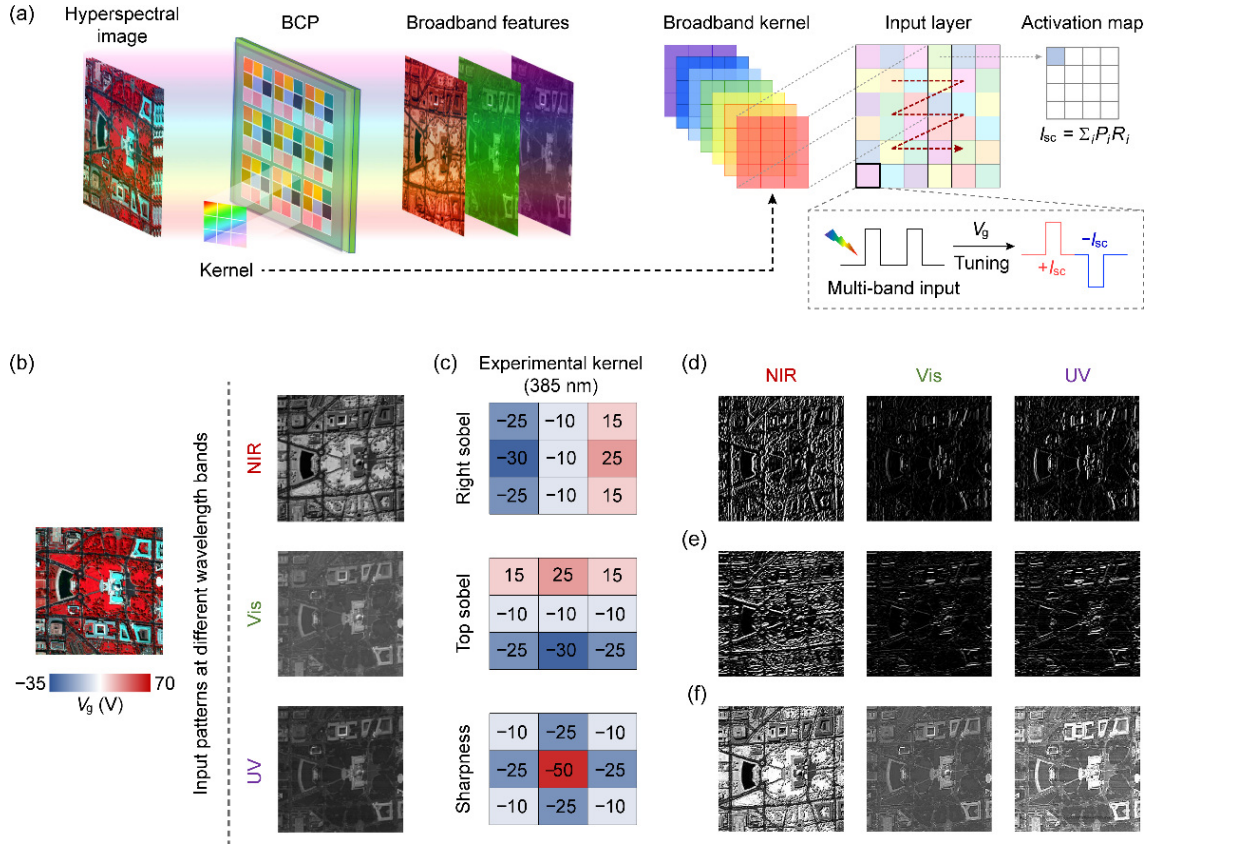

Figure 4 Implementation of in-sensor BCP using the TAC-$PtSe_2$/WSe_2 photovoltaic device. (a) Schematic illustration of the in-sensor BCP process and operation mechanism. (b) Input original images of Washington D.C. mall (https://rslab.ut.ac.ir/data) with UV, visible, and NIR wavelengths. (c) The experimental kernels obtained from V_g under 385 nm light illumination for illustration. Demonstration of (d) vertical edge detection, (e) horizontal edge detection, and (f) sharpness of the hyperspectral image of Washington D.C. mall at different wavelength bands.

can be encoded by the incident light power P_i. The output photocurrent I_{sc} is expressed as $\Sigma_i P_i R_i$, where R_i is the photoresponsivity of the device, representing the weight in the BCP. Thus, the photoresponsivity of the device can be modulated through varying V_g to realize the configurations of different kernels for the specific convolution processes, in which the broadband characteristics are represented by the wavelength-dependent photovoltaic response features.

A hyperspectral image from the Washington D.C. mall dataset is used to conceptually illustrate the various convolution operations, where a single device is used to receive information in a pixel-by-pixel manner. The images belonging to each individual wavelength band (i.e., UV, visible, and NIR) are extracted and displayed (Fig. 4(b)), where the information contained in each pixel is detected by the photovoltaic device at V_g = 0 V, generating a series of photocurrent that represents the input patterns in the grey scale. As shown in Fig. 4(c), three experimentally obtained kernels (right/top edge detection and sharpening) in terms of V_g at the wavelength of 385 nm are selected for illustration, with the corresponding photoresponsivity matrix shown in Fig. S17(a) in the ESM. Kernels obtained for other wavelengths (520 and 980 nm) are demonstrated in Figs. S17(b) and S17(c) in the ESM. Figures 4(d)–4(f) display the output images at different wavelength bands after the operations of right/top edge detection and sharpening, respectively. Note that the edge detection is observed as eliminating the black/white contrast in a pattern, while the sharpening is manifested as enhancing the hidden information in the under-/over-exposed regions of the target remote sensing scenes. The experimental results show good agreement with the ideal output generated by using the software kernels (Fig. S18 in the ESM), indicating the superiority of the photovoltaic device in processing hyperspectral remote sensing images. On the other hand, through deliberately designing and tuning the device, we expect the realization of programmable and non-volatile characteristics, which would demonstrate the potential in achieving dynamic signal processing as reported previously [52].

4 Conclusions

In summary, we have reported a TAC-assisted synthesis strategy of high-quality 2D $PtSe_2$ that demonstrates low thermal budget with robust CMOS compatibility. By utilizing the metallic nature of TAC-$PtSe_2$, we fabricate a TAC-$PtSe_2$/WSe_2 heterostructure based Schottky diode with broadband photovoltaic response characteristics. The gate-tunable band alignment configurations in the heterostructure facilitate the positive-to-negative polarity switching of the photoresponsivity across a wide wavelength range, which is essential for constructing various convolution kernels for different operations. We thus utilize the device to implement the convolutional operations of edge detection and sharpening on the hyperspectral image of Washington D.C. mall, where the results are of comparable quality as those obtained by using ideal software kernels. Our approach envisions a reliable strategy for the fabrication of 2D heterostructure based Schottky diode with tunable band alignment, paving the way to achieve broadband in-sensor visual information processing in CMOS compatible manner.

Electronic Supplementary Material: Supplementary material (the relationship between selenization time and Pt thickness; Raman intensity mapping, Raman polar plots, ARPRS, and XPS spectra of TAC-$PtSe_2$ films; schematic illustration of TLM measurements; R_c and R_{sh} of the TAC-$PtSe_2$ transistor derived from 4 nm Pt layer; optical image, output, and transfer characteristics of the TAC-$PtSe_2$ transistors; Raman spectra and rectification ratio of the TAC-$PtSe_2$/WSe_2 device; site-specific photoresponse, photoresponse speed, and cyclic endurance of the TAC-$PtSe_2$/WSe_2 device; the WSe_2 channels fabricated without and with selenization, as well as their transfer characteristics; photovoltaic performance (1064 nm) of the TAC-$PtSe_2$/WSe_2 device; R_{sc} of TAC-$PtSe_2$/WSe_2 devices with thinner WSe_2; the experimentally obtained convolution kernels; simulation results of the edge detection and sharpness) is available in the online version of this article at https://doi.org/10.26599/NR.2025.94907049.

Data availability

All data needed to support the conclusions in the paper are presented in the manuscript and the Electronic Supplementary Material. Additional data related to this paper may be requested from the corresponding author upon request.

Acknowledgements

Authors acknowledge the financial support from the National Key R&D Program of China (No. 2023YFA1407800), the National Natural Science Foundation of China (Nos. 62104041, 62374038, and 62204051), the Shanghai Sailing Program (No. 21YF1402600), the Natural Science Foundation of Shanghai (No. 22ZR1405700), and the Shanghai Rising-Star Program (No. 22QA1401000).

Declaration of competing interest

All the contributing authors report no conflict of interests in this work.

Author contribution statement

Z. C. H.: Writing – review & editing, writing – origin draft, methodology, investigation, formal analysis, data curation, validation. S. J. T.: Methodology, formal analysis, data curation, validation. H. W.: Methodology, investigation, formal analysis. W. H. S.: Investigation, data curation. Y. G.: Investigation, data curation. Y. C.: Methodology, investigation. F. X. T.: Formal analysis, data curation. H. H. L.: Investigation, data curation. T. H. W.: Data curation. Y. Y.: Investigation. W. Y. S. L.: Investigation. Y. W.: Investigation. T. L.: Writing – review & editing, methodology, software, supervision, resources, project administration, investigation, funding acquisition, conceptualization. D. X.: Writing – review & editing, methodology, supervision, resources, project administration, investigation, funding acquisition, conceptualization. All the authors have approved the final manuscript.

Use of AI statement

None.

References

[1] Seo, S. Y.; Moon, G.; Okello, O. F. N.; Park, M. Y.; Han, C.; Cha, S.; Choi, H.; Yeom, H. W.; Choi, S. Y.; Park, J. et al. Reconfigurable photo-induced doping of two-dimensional van der Waals semiconductors using different photon energies. *Nat. Electron.* **2020**, *4*, 38–44.

[2] Zhou, F. C.; Zhou, Z.; Chen, J. W.; Choy, T. H.; Wang, J. L.; Zhang, N.; Lin, Z. Y.; Yu, S. M.; Kang, J. F.; Wong, H. S. P. et al. Optoelectronic resistive random access memory for neuromorphic vision sensors. *Nat. Nanotechnol.* **2019**, *14*, 776–782.

[3] Feng, X. X.; He, L. X.; Cheng, Q. M.; Long, X. Y.; Yuan, Y. X. Hyperspectral and multispectral remote sensing image fusion based on endmember spatial information. *Remote Sens.* **2020**, *12*, 1009.

[4] Zhang, Y. C.; Wang, L. M.; Lei, Y. Y.; Wang, B.; Lu, Y.; Yao, Y. Y.; Zhang, N. N.; Lin, D. D.; Jiang, Z. M.; Guo, H. et al. Self-powered bidirectional photoresponse in high-detectivity WSe_2 phototransistor with asymmetrical van der Waals stacking for retinal neurons emulation. *ACS Nano* **2022**, *16*, 20937–20945.

[5] Wang, C. Y.; Liang, S. J.; Wang, S.; Wang, P. F.; Li, Z.; Wang, Z. R.; Gao, A. Y.; Pan, C.; Liu, C.; Liu, J. et al. Gate-tunable van der Waals heterostructure for reconfigurable neural network vision sensor. *Sci. Adv.* **2020**, *6*, eaba6173.

[6] Ham, D.; Park, H.; Hwang, S.; Kim, K. Neuromorphic electronics based on copying and pasting the brain. *Nat. Electron.* **2021**, *4*, 635–644.

[7] Jayachandran, D.; Oberoi, A.; Sebastian, A.; Choudhury, T. H.; Shankar, B.; Redwing, J. M.; Das, S. A low-power biomimetic collision detector based on an in-memory molybdenum disulfide photodetector. *Nat. Electron.* **2020**, *3*, 646–655.

[8] Roy, K.; Jaiswal, A.; Panda, P. Towards spike-based machine intelligence with neuromorphic computing. *Nature* **2019**, *575*, 607–617.

[9] Feldmann, J.; Youngblood, N.; Karpov, M.; Gehring, H.; Li, X.; Stappers, M.; Le Gallo, M.; Fu, X.; Lukashchuk, A.; Raja, A. S. et al. Parallel convolutional processing using an integrated photonic tensor core. *Nature* **2021**, *589*, 52–58.

[10] Pi, L. J.; Wang, P. F.; Liang, S. J.; Luo, P.; Wang, H. Y.; Li, D. Y.; Li, Z. X.; Chen, P.; Zhou, X.; Miao, F. et al. Broadband convolutional processing using band-alignment-tunable heterostructures. *Nat. Electron.* **2022**, *5*, 248–254.

[11] Brown, C. B.; Remelius, D. K.; Smilowitz, L. B. Evaluation of silicon and indium gallium arsenide photodiodes as direct timing detectors for pulsed X-ray systems. *Rev. Sci. Instrum.* **2024**, *95*, 033102.

[12] Lee, S.; Peng, R. M.; Wu, C. M.; Li, M. Programmable black phosphorus image sensor for broadband optoelectronic edge computing. *Nat. Commun.* **2022**, *13*, 1485.

[13] Gao, A. Y.; Lai, J. W.; Wang, Y. J.; Zhu, Z.; Zeng, J. W.; Yu, G. L.; Wang, N. Z.; Chen, W. C.; Cao, T. J.; Hu, W. D. et al. Observation of ballistic avalanche phenomena in nanoscale vertical InSe/BP heterostructures. *Nat. Nanotechnol.* **2019**, *14*, 217–222.

[14] Burr, G. W. A role for analogue memory in AI hardware. *Nat. Mach. Intell.* **2019**, *1*, 10–11.

[15] Jang, H.; Liu, C. Y.; Hinton, H.; Lee, M. H.; Kim, H.; Seol, M.; Shin, H. J.; Park, S.; Ham, D. An atomically thin optoelectronic machine vision processor. *Adv. Mater.* **2020**, *32*, 2002431.

[16] Lee, J.; Duong, N. T.; Bang, S.; Park, C.; Nguyen, D. A.; Jeon, H.; Jang, J.; Oh, H. M.; Jeong, M. S. Modulation of junction modes in $SnSe_2$/$MoTe_2$ broken-gap van der Waals heterostructure for multifunctional devices. *Nano Lett.* **2020**, *20*, 2370–2377.

[17] Zhang, X. K.; Liu, B. S.; Gao, L.; Yu, H. H.; Liu, X. Z.; Du, J. L.; Xiao, J. K.; Liu, Y. H.; Gu, L.; Liao, Q. L. et al. Near-ideal van der Waals rectifiers based on all-two-dimensional Schottky junctions. *Nat. Commun.* **2021**, *12*, 1522.

[18] Huang, H. F.; Xu, W. S.; Chen, T. X.; Chang, R. J.; Sheng, Y. W.; Zhang, Q. Y.; Hou, L. L.; Warner, J. H. High-performance two-dimensional Schottky diodes utilizing chemical vapour deposition-grown graphene-MoS_2 heterojunctions. *ACS Appl. Mater. Interfaces* **2018**, *10*, 37258–37266.

[19] Singh, A.; Uddin, M. A.; Sudarshan, T.; Koley, G. Tunable reverse-biased graphene/silicon heterojunction Schottky diode sensor. *Small* **2014**, *10*, 1555–1565.

[20] Di Bartolomeo, A. Graphene schottky diodes: An experimental review

of the rectifying graphene/semiconductor heterojunction. *Phys. Rep.* **2016**, *606*, 1–58.
[21] Guo, P. W.; Jia, M. M.; Guo, D.; Wang, Z. L.; Zhai, J. Y. Retina-inspired in-sensor broadband image preprocessing for accurate recognition via the flexophototronic effect. *Matter* **2023**, *6*, 537–553.
[22] Wang, S. J.; Qi, L. G.; Xia, Z. H.; Wang, W. H.; Yue, D. W.; Wang, S. P.; Su, S. C. Polarization-sensitive detector based on $MoTe_2$/WTe_2 heterojunction for broadband optoelectronic imaging. *J. Phys. Chem. Lett.* **2023**, *14*, 10509–10516.
[23] Zhang, N.; Wang, F. K.; Li, P. Y.; Liang, Y.; Luo, H.; Ouyang, D. C.; Luo, L. B.; Wu, J. S.; Zhao, Y. H.; Li, Y. et al. Two-dimensional vertical-lateral hybrid heterostructure for ultrasensitive photodetection and image sensing. *Mater. Today* **2023**, *69*, 79–87.
[24] Pan, X.; Shi, J. W.; Wang, P. F.; Wang, S.; Pan, C.; Yu, W. T.; Cheng, B.; Liang, S. J.; Miao, F. Parallel perception of visual motion using light-tunable memory matrix. *Sci. Adv.* **2023**, *9*, eadi4083.
[25] Yoon, H. H.; Fernandez, H. A.; Nigmatulin, F.; Cai, W. W.; Yang, Z. Y.; Cui, H. X.; Ahmed, F.; Cui, X. Q.; Uddin, M. G.; Minot, E. D. et al. Miniaturized spectrometers with a tunable van der Waals junction. *Science* **2022**, *378*, 296–299.
[26] Liu, P.; Xiang, B. 2D hetero-structures based on transition metal dichalcogenides: Fabrication, properties and applications. *Sci. Bull.* **2017**, *62*, 1148–1161.
[27] Wang, F. K.; Hu, F. C.; Dai, M. J.; Zhu, S.; Sun, F. Y.; Duan, R. H.; Wang, C. W.; Han, J. Y.; Deng, W. J.; Chen, W. D. et al. A two-dimensional mid-infrared optoelectronic retina enabling simultaneous perception and encoding. *Nat. Commun.* **2023**, *14*, 1938.
[28] Zeng, Y. H.; Meng, F. X.; Fan, S. D.; Wang, P. F.; Kou, C. Y.; Sun, M. Y.; Hu, H. G.; Cao, R.; Wageh, S.; Al-Hartomy, O. A. et al. Fully depleted vdW heterojunction based high performance photovoltaic photodetector. *J. Materiomics* **2023**, *9*, 1039–1047.
[29] Wu, G. J.; Zhang, X. M.; Feng, G. D.; Wang, J. L.; Zhou, K. J.; Zeng, J. H.; Dong, D. N.; Zhu, F. D.; Yang, C. K.; Zhao, X. M. et al. Ferroelectric-defined reconfigurable homojunctions for in-memory sensing and computing. *Nat. Mater.* **2023**, *22*, 1499–1506.
[30] Shawkat, M. S.; Chung, H. S.; Dev, D.; Das, S.; Roy, T.; Jung, Y. Two-dimensional/three-dimensional Schottky junction photovoltaic devices realized by the direct CVD growth of vdW 2D $PtSe_2$ layers on silicon. *ACS Appl. Mater. Interfaces* **2019**, *11*, 27251–27258.
[31] Mc Manus, J. B.; Cunningham, G.; McEvoy, N.; Cullen, C. P.; Gity, F.; Schmidt, M.; McAteer, D.; Mullarkey, D.; Shvets, I. V.; Hurley, P. K. et al. Growth of 1T' $MoTe_2$ by thermally assisted conversion of electrodeposited tellurium films. *ACS Appl. Energy Mater.* **2019**, *2*, 521–530.
[32] Gatensby, R.; Hallam, T.; Lee, K.; McEvoy, N.; Duesberg, G. S. Investigations of vapour-phase deposited transition metal dichalcogenide films for future electronic applications. *Solid-State Electron.* **2016**, *125*, 39–51.
[33] Gatensby, R.; McEvoy, N.; Lee, K.; Hallam, T.; Berner, N. C.; Rezvani, E.; Winters, S.; O'Brien, M.; Duesberg, G. S. Controlled synthesis of transition metal dichalcogenide thin films for electronic applications. *Appl. Surf. Sci.* **2014**, *297*, 139–146.
[34] Yuan, J.; Sun, T.; Hu, Z. X.; Yu, W. Z.; Ma, W. L.; Zhang, K.; Sun, B. Q.; Lau, S. P.; Bao, Q. L.; Lin, S. H. et al. Wafer-scale fabrication of two-dimensional PtS_2/$PtSe_2$ heterojunctions for efficient and broad band photodetection. *ACS Appl. Mater. Interfaces* **2018**, *10*, 40614–40622.
[35] Wang, G. Z.; Wang, K. P.; McEvoy, N.; Bai, Z. Y.; Cullen, C. P.; Murphy, C. N.; McManus, J. B.; Magan, J. J.; Smith, C. M.; Duesberg, G. S. et al. Ultrafast carrier dynamics and bandgap renormalization in layered $PtSe_2$. *Small* **2019**, *15*, 1902728.
[36] Yim, C.; McEvoy, N.; Riazimehr, S.; Schneider, D. S.; Gity, F.; Monaghan, S.; Hurley, P. K.; Lemme, M. C.; Duesberg, G. S. Wide spectral photoresponse of layered platinum diselenide-based photodiodes. *Nano Lett.* **2018**, *18*, 1794–1800.
[37] Yu, X. C.; Yu, P.; Wu, D.; Singh, B.; Zeng, Q. S.; Lin, H.; Zhou, W.; Lin, J. H.; Suenaga, K.; Liu, Z. et al. Atomically thin noble metal dichalcogenide: A broadband mid-infrared semiconductor. *Nat. Commun.* **2018**, *9*, 1545.
[38] Huang, H. Q.; Zhou, S. Y.; Duan, W. H. Type-II Dirac fermions in the $PtSe_2$ class of transition metal dichalcogenides. *Phys. Rev. B* **2016**, *94*, 121117.
[39] Han, S. S.; Kim, J. H.; Noh, C.; Kim, J. H.; Ji, E.; Kwon, J.; Yu, S. M.; Ko, T. J.; Okogbue, E.; Oh, K. H. et al. Horizontal-to-vertical transition of 2D layer orientation in low-temperature chemical vapor deposition-grown $PtSe_2$ and its influences on electrical properties and device applications. *ACS Appl. Mater. Interfaces* **2019**, *11*, 13598–13607.
[40] Agnihotri, P.; Dhakras, P.; Lee, J. U. Bipolar junction transistors in two-dimensional WSe_2 with large current and photocurrent gains. *Nano Lett.* **2016**, *16*, 4355–4360.
[41] Michael, A.; Chuang, I. Y. H.; Kwok, C. Y.; Omaki, K. Low-thermal-budget electrically active thick polysilicon for CMOS-first MEMS-last integration. *Microsyst. Nanoeng.* **2024**, *10*, 75.
[42] Yim, C.; Passi, V.; Lemme, M. C.; Duesberg, G. S.; Ó Coileáin, C.; Pallecchi, E.; Fadil, D.; McEvoy, N. Electrical devices from top-down structured platinum diselenide films. *npj 2D Mater. Appl.* **2018**, *2*, 5.
[43] Jiang, K.; Cui, A. Y.; Shao, S.; Feng, J. J.; Dong, H. L.; Chen, B.; Wang, Y. C.; Hu, Z. G.; Chu, J. H. New pressure stabilization structure in two-dimensional $PtSe_2$. *J. Phys. Chem. Lett.* **2020**, *11*, 7342–7349.
[44] Yim, C.; Lee, K.; McEvoy, N.; O'Brien, M.; Riazimehr, S.; Berner, N. C.; Cullen, C. P.; Kotakoski, J.; Meyer, J. C.; Lemme, M. C. et al. High-performance hybrid electronic devices from layered $PtSe_2$ films grown at low temperature. *ACS Nano* **2016**, *10*, 9550–9558.
[45] Setiyawati, I.; Chiang, K. R.; Ho, H. M.; Tang, Y. H. Distinct electronic and transport properties between 1T-$HfSe_2$ and 1T-$PtSe_2$. *Chin. J. Phys.* **2019**, *62*, 151–160.
[46] Gao, Y.; Hong, Y. L.; Yin, L. C.; Wu, Z. T.; Yang, Z. Q.; Chen, M. L.; Liu, Z. B.; Ma, T.; Sun, D. M.; Ni, Z. H. et al. Ultrafast growth of high-quality monolayer WSe_2 on Au. *Adv. Mater.* **2017**, *29*, 1700990.
[47] Prakash, A.; Appenzeller, J. Bandgap extraction and device analysis of ionic liquid gated WSe_2 Schottky barrier transistors. *ACS Nano* **2017**, *11*, 1626–1632.
[48] Wang, X. X.; Wang, S. F.; Wu, Y. W.; Wang, W. H.; Cao, Z. Y.; Wei, B. B.; Han, T.; Li, F.; Wang, S. L.; Shan, L. et al. A self-powered photodetector based on graphene enhanced WSe_2/$PtSe_2$ heterodiode with fast speed and broadband response. *Adv. Opt. Mater.* **2024**, *12*, 2400052.
[49] Ouyang, B. S.; Wang, J. L.; Zeng, G.; Yan, J. M.; Zhou, Y.; Jiang, X. X.; Shao, B. J.; Chai, Y. Bioinspired in-sensor spectral adaptation for perceiving spectrally distinctive features. *Nat. Electron.,* **2024**, *7*, 705–713.
[50] Wu, D.; Wang, Y. G.; Zeng, L. H.; Jia, C.; Wu, E. P.; Xu, T. T.; Shi, Z. F.; Tian, Y. T.; Li, X. J.; Tsang, Y. H. Design of 2D layered $PtSe_2$ heterojunction for the high-performance, room-temperature, broadband, infrared photodetector. *ACS Photonics* **2018**, *5*, 3820–3827.
[51] Choi, C.; Leem, J.; Kim, M.; Taqieddin, A.; Cho, C.; Cho, K. W.; Lee, G. J.; Seung, H.; Bae, H. J.; Song, Y. M. et al. Curved neuromorphic image sensor array using a MoS_2-organic heterostructure inspired by the human visual recognition system. *Nat. Commun.* **2020**, *11*, 5934.
[52] Zhou, Y.; Fu, J. W.; Chen, Z. R.; Zhuge, F. W.; Wang, Y. S.; Yan, J. M.; Ma, S. J.; Xu, L.; Yuan, H. M.; Chan, M. et al. Computational event-driven vision sensors for in-sensor spiking neural networks. *Nat. Electron.* **2023**, *6*, 870–878.